

AALTO UNIVERSITY
School of Engineering
Department of Energy Technology

Arttu Meriläinen

Experimental and theoretical studies of energy efficient convective heat transfer, mass transfer and heat storage

Licentiate thesis submitted in partial fulfillment of the requirements for the degree of Licentiate of Science in Technology

Espoo, January 7, 2013

Supervisor: Professor Markku Lampinen

Advisor: Ari Seppälä, D.Sc. (Tech.)

Author	Arttu Meriläinen	
Title of thesis	Experimental and theoretical studies of energy efficient convective heat transfer, mass transfer and heat storage	
Department	Department of Energy Technology	
Field of research	Energy Engineering IA015Z	
Supervising professor	Markku Lampinen	Code of professorship Ene-39
Thesis advisor	Ari Seppälä, D.Sc. (Tech.)	
Thesis examiners	Esa Muurinen, D.Sc. (Tech.) and Professor Markku Lampinen	
Date	January 7, 2013	Number of pages 35+37
		Language english

Abstract

Convective heat transfer enhancement by nanofluids, oxygen-enrichment by polymeric membranes and crystallization of supercooled xylitol are studied.

A nanofluid is a suspension of ultrafine particles (<100 nm) in a conventional base fluid. Turbulent convective heat transfer and pressure drop of several well characterized water-based Al₂O₃-, SiO₂- and MgO-nanofluids with a nanoparticle volume fraction up to 4.0 % were studied experimentally. Average convective heat transfer coefficients are significantly enhanced when compared to the base fluid on the basis of constant Reynolds number. An increase of over 40 % was observed for several nanofluids. One of the main results is that for many nanofluids the heat transfer efficiency is lower than that of the base fluid, although the bare heat transfer coefficients are significantly larger. It is shown that this is due to the fact that when nanoparticles are added to the base fluid, a competition between the heat transfer augmentation and increased pressure losses is imminent. When the pressure losses are properly accounted for, only one of the nanofluids studied here, namely a SiO₂ based nanofluid with a small concentration of smooth spherical particles (of average size 6.5±1.8 nm), shows noticeable improvement in heat transfer as compared to the base fluid. This highlights the importance of characterizing the nature of the particle phase in heat transfer experiments of nanofluids.

The energy efficiency of the separation of air into an oxygen-enriched permeate and an oxygen-depleted residue stream in a polymeric hollow fiber membrane module is studied. A model is developed to simulate the separation of gases in counter-current lumen-feed flow. The vacuum permeate configuration, where a vacuum is maintained on the permeate side of the membrane, is the most efficient single-stage process. A two-stage configuration, where the permeate of the first module is further enriched in a second stage, is also considered. By optimizing both stages the specific energy consumption can, in some cases, be further reduced. The optimization of the module geometry is not as important as the optimization of the feed parameters – the pressure ratio and stage cut. Radically decreasing the membrane thickness decreases energy efficiency due to an increased influence of concentration polarization and higher pressure losses. Present-day polymeric membrane modules can compete with traditional techniques in specific energy consumption when the required oxygen molar fraction is low.

Supercooled phase change materials can be used in special long-term heat storage applications. The discharge of the stored latent heat can be started at will in temperatures below the crystallization temperature. Xylitol's high specific latent heat and non-corrosiveness make it a candidate for such a material. It can be easily supercooled to room temperature and below (the melting temperature of pure xylitol is about 92 °C). However, the speed of crystallization is low leading to a low release rate of the stored latent heat. Several additives are experimentally studied with the objective of increasing the speed of crystallization by reducing the interfacial tension between solid and liquid phases at the crystallization front and by reducing the viscosity of the liquid phase. The highest velocities of the crystallization front in room temperature were achieved with methanol as an additive. Compared to pure xylitol the crystallization front velocities were up to 33 times higher in vertical experiments and up to 170 times higher in horizontal experiments.

Keywords nanofluid, nanoparticles, convective heat transfer, viscosity, pressure loss, oxygen enrichment, membrane, hollow fiber module, energy efficiency, heat storage, supercooling, crystallization, xylitol

Tekijä Arttu Meriläinen

Työn nimi Tutkimuksia energiatehokkaista lämmön- ja aineensiirtomenetelmistä sekä lämmönvarastoinnista

Laitos Energiatekniikan laitos

Tutkimusala Energiatekniikka IA015Z

Vastuuprofessori Markku Lampinen**Professuurikoodi** Ene-39

Työn ohjaaja TkT Ari Seppälä

Työn tarkastajat TkT Esa Muurinen ja professori Markku Lampinen

Päivämäärä 7.1.2013**Sivumäärä** 35+37**Kieli** englanti

Tiivistelmä

Työ sisältää tutkimuksia nanonesteiden konvektiivisesta lämmönsiirrosta, hapen rikastamisesta polymeeristen kalvojen avulla sekä alijäähtyneen ksylitolin kiteytymisestä.

Nanonesteillä tarkoitetaan vähintään kaksikomponenttistä systeemiä, jossa nanopartikkeleita (<100 nm) on liuotettu puhtaaseen nesteeseen. Työssä selvitetään kokeellisesti Al₂O₃-, SiO₂- ja MgO-nanonesteiden ominaisuuksia konvektiivisessa lämmönsiirrosta. Monilla nanonesteillä mitatut keskimääräiset lämmönsiirtokertoimet ovat yli 40% paremmat kuin puhtaalla vedellä, kun vertailu tehdään samalla Reynoldsin luvulla. Tästä huolimatta monen nanonesteen lämmönsiirtotehokkuus on puhdasta vettä alhaisempi. Kun veteen lisätään nanopartikkeleita, kasvavat lämmönsiirtokertoimien lisäksi nesteen dynaaminen viskositeetti sekä virtauksen painehäviöt. Kun painehäviöt otetaan huomioon, tutkituista nanonesteistä ainoastaan yhden (SiO₂, partikkelien muoto pyöreä, koko 6.5±1.8 nm) tulokset olivat parempia myös lämmönsiirtotehokkuudessa, mikä korostaa nanopartikkelien huolellisen karakterisoinnin merkitystä.

Työssä tutkitaan hapen rikastamista polymeerikalvojen avulla. Prosessissa ilma erotetaan onttokuitumoduulissa happirikkaaksi permeaatiksi ja typpirikkaaksi retentaatiksi. Mallinnettua vastavirtaprosessia optimoidaan säätämällä painetasoja ja kaasuvirtauksia tavoitteena ominaisenergiankulutuksen minimoiminen. Permeaatin alipaineistaminen on energiatehokkain yksivaiheinen konfiguraatio. Optimoitu kaksivaiheinen erotusprosessi, jossa ensimmäisen vaiheen permeaatti rikastetaan uudellaan toisessa moduulissa, on tietyissä tapauksissa vieläkin tehokkaampi. Energiatehokkuuden kannalta moduuligeometrian optimointi ei ole yhtä tärkeää kuin painetasojen ja kaasuvirtausten. Membraanikalvon radikaali ohentaminen johtaa huonompaan energiatehokkuuteen. Syitä tähän ovat kaasuvirtausten kohonneet painehäviöt sekä kohonnut konsentraatiopolarisaation vaikutus. Polymeerikalvojen avulla on mahdollista tuottaa happirikkaa ilmaa pienellä ominaisenergiankulutuksella, kun tarvittava happipitoisuus on pieni.

Faasimuutosmateriaalien alijäähtymistä voidaan hyödyntää pitkäaikaisessa lämmönvarastoinnissa. Alijäähtyneeseen nesteeseen varastoitua faasimuutoslämpöä voidaan säilyttää häviöttä pitkiä aikoja ja vapauttaa haluttaessa. Ksylitolilla on korkea faasimuutoslämpö sekä hyvät alijäähtymisominaisuudet. Ksylitoli (sulamispiste 92 °C) alijäähtyy helposti huoneenlämpöön, mutta kiteytyminen ja siten faasimuutoslämmön vapautuminen ovat erittäin hitaita. Ksylitolin kiteytymisrintaman nopeutta pyrittiin kasvattamaan eri lisäaineiden avulla eri lämpötiloissa. Kiteytymisnopeuteen pyrittiin vaikuttamaan pienentämällä pintajännitystä nestefaasin ja kiinteän faasin välillä sekä pienentämällä nestemäisen ksylitolin viskositeettia. Suurimmat parannukset saatiin metanolin avulla. Kiteytymisrintaman nopeus pystysuorissa kokeissa kasvoi parhaimmillaan 33-kertaiseksi ja vaakasuorissa kokeissa parhaimmillaan 170-kertaiseksi.

Avainsanat nanoneste, nanopartikkeli, konvektiivinen lämmönsiirto, viskositeetti, painehäviöt, hapen rikastaminen, membraani, onttokuitumoduuli, energiatehokkuus, lämpövarasto, alijäähtyminen, kiteytyminen, ksylitoli

Foreword

This work was carried out during the years 2008-2012 in the Department of Energy Technology in Aalto University's School of Engineering. Paper I was funded in part by the Finnish Funding Agency for Technology and Innovation (TEKES) FinNano program (project NanoTermo), the Academy of Finland (NanoFluid Consortium grant and Metafluid project (decision no. 132442)) and the Strategic Centre of Science, Technology and Innovation (Cleen Ltd., EFEU-program). Paper I was also supported by the Academy of Finland through its Centre of Excellence Program (project no. 251748 COMP). Paper II is part of the project Oxygen Carriers and Their Industrial Applications, funded by the Finnish Funding Agency for Technology and Innovation (TEKES) Functional Materials Programme, Foster Wheeler Energia Oy and Fortum Oyj. Paper III was funded by the TEKES ClimBus-research program (project PCMAkku) and Danisco Sweeteners.

I would like to take this opportunity to thank a group of people who have supported and guided me throughout the course of this study. I wish to express my sincere thanks to Ari Seppälä for introducing me to the world of scientific research. His diligent guidance was nothing less than essential. Professor Tapio Ala-Nissilä and Kari Saari helped tremendously in Paper I. Special thanks to my supervisor, Professor Markku Lampinen, and Maunu Kuosa for their encouragement and generous support during the many months of pitfalls and setbacks. I wish to thank laboratory technician Mika Ahlgren for his help in constructing the experimental apparatus and the whole Applied Thermodynamics crew for interesting lectures and courses over the years and for a relaxed working atmosphere.

Finally, I would like to extend my thanks to my fiancée Johanna, my parents, sisters, and great friends.

Espoo, January 7, 2013

Arttu Meriläinen

Table of contents

ABSTRACT (eng.).....	2
ABSTRACT (fin.)	3
FOREWORD.....	4
NOMENCLATURE.....	6
LIST OF PUBLICATIONS.....	8
1. INTRODUCTION.....	9
2. EXPERIMENTAL STUDY OF TURBULENT CONVECTIVE HEAT TRANSFER AND PRESSURE DROP OF WATER BASED OXIDE NANOFLUIDS INSIDE A CIRCULAR TUBE.....	11
2.1 Characterization of nanofluids.....	12
2.1.1 Particle size distributions.....	12
2.1.2 Particle shapes.....	12
2.1.3 Viscosity measurements and physical properties.....	12
2.2 Experimental setup.....	13
2.2.1 Turbulent convective heat transfer coefficient.....	14
2.3 Convective heat transfer enhancement in turbulent flow using nanofluids	14
2.3.1 Heat transfer coefficients	14
2.3.2 Pressure losses.....	16
2.3.3 Efficiency of convective heat transfer.....	16
2.4 Conclusions.....	18
3. MINIMIZING SPECIFIC ENERGY CONSUMPTION OF OXYGEN ENRICHMENT IN POLYMERIC HOLLOW FIBER MEMBRANE MODULES.....	20
3.1 Model development.....	20
3.1.1 Fiber model.....	21
3.2 Specific energy consumption of membrane air separation.....	22
3.3 Results and discussion.....	24
3.3.1 Effects of selectivity α , pressure ratio ϕ , and stage cut θ oxygen enrichment.....	24
3.3.2 Influence of flow parameters on the specific energy consumption e	24
3.3.3 Influence of the module geometry on the specific energy consumption e	25
3.3.4 Comparison of system configurations.....	26
3.4 Conclusions.....	27
4. IMPROVING THE HEAT DISCHARGE RATE OF A THERMAL STORAGE BASED ON SUPERCOOLED XYLITOL.....	29
4.1 Experimental methods.....	29
4.2 Results.....	29
4.2.1 Propagation of the crystallization front at room temperature.....	29
4.2.2 Methanol as an additive.....	30
4.2.3 The effect of temperature on the speed of the crystallization front.....	31
4.2.4 Long-term durability in a supercooled state.....	32
4.3 Conclusions.....	32
5. SUMMARY.....	33
5.1 Main results.....	33
5.2 Discussion and future outlook.....	34
REFERENCES.....	35

Nomenclature

A_{cs}	cross-sectional area, m^2
A_{eff}	effective membrane area, m^2
b	permeability, m^2/s
c_p	specific heat capacity, $J/(kg \cdot K)$
d	diameter, m
d_h	hydraulic diameter, m
d_{in}	inner diameter, m
d_m	module inner diameter, m
d_{out}	outer diameter, m
D	diffusion coefficient, m^2/s
e	specific energy consumption, $J/mol(O_2)$
f	friction factor, -
f	module packing factor, -
G	conductance, W/K
G'	conductance per unit length, $W/(m \cdot K)$
ΔG^*	energy barrier, J
ΔG_v	Gibbs free energy between phases, J
h	heat transfer coefficient, $W/(m^2 \cdot K)$
k	thermal conductivity, $W/(m \cdot K)$
K	ball constant, m^2/s^2
K	overall mass transfer coefficient, m/s
L	length, m
\dot{m}	mass flow rate, kg/s
\dot{m}_i	mass flux, $kg/(m^2 \cdot s)$
M	molar mass, kg/mol
\dot{n}	molar flow rate, mol/s
N_f	number of fibers, -
Nu	Nusselt number ($Nu = hd/k$), -
p	pressure, Pa
p_i	partial pressure, Pa
P	power, W
Pr	Prandtl number ($Pr = c_p \mu / k$), -
R	total mass transfer resistance, s/m
R_g	universal gas constant, $J/(mol \cdot K)$
Re	Reynolds number ($Re = \rho u d / \mu$), -
S	solubility, $mol/(m^3 \cdot Pa)$
Sc	Schmidt number, -
Sh	Sherwood number, -
t	time, s
T	temperature, K
u	axial velocity, m/s
U	wetted perimeter, m
v	radial velocity, m/s
\dot{V}	volumetric flow rate, m^3/s
x	molar fraction, -
z	axial length, m
α	selectivity, -
γ	interfacial energy
δ	membrane thickness, m
ε	absolute surface roughness, m
η	convective heat transfer efficiency, -
θ	stage cut, -
θ_{ln}	logarithmic temperature difference, K
μ	dynamic viscosity, $kg/(m \cdot s)$
η	efficiency, -
ρ	density, kg/m^3
φ	volume fraction, -

ϕ heat transfer rate, W
 ϕ pressure ratio, -

Subscripts

bf base fluid
comp compressor
f fluid
feed feed
g generator
in inner
l lumen
nf nanofluid
o outer
p particle
perm permeate
pne pneumatic motor
res residue
s surface
s shell
st steam
vac vacuum pump

List of publications

This thesis consists of a review of the following three studies, which are subsequently referred to as Papers I-III.

I

A. Meriläinen, A. Seppälä, K. Saari, J. Seitsonen, J. Ruokolainen, S. Puisto, N. Rostedt and T. AlaNissila, Influence of particle size and shape on turbulent heat transfer characteristics and pressure losses in water-based nanofluids, under review in *International Journal of Heat and Mass Transfer* (2012).

II

A. Meriläinen, A. Seppälä and P. Kauranen, Minimizing specific energy consumption of oxygen enrichment in polymeric hollow fiber membrane modules, *Applied Energy* **94** (2012).

III

A. Seppälä, A. Meriläinen, L. Wikström and P. Kauranen, The effect of additives on the speed of the crystallization front of xylitol with various degrees of supercooling, *Experimental Thermal and Fluid Science* **34** (2010).

1. Introduction

The demand for energy can be decreased by improvements in energy efficiency that are achieved by utilizing more efficient technologies or processes. Gains in energy efficiency are a priority for a more sustainable energy future and more often than not these gains are the fastest and most cost-effective way to reduce emissions and diminish energy demands.

Nanofluids - a new class of solid-liquid composite materials consisting of nanoparticles in a liquid - have the potential to increase the heat transfer properties of their base fluids. Their enhanced properties are highlighted by reports on significant enhancement of thermal transport properties at modest nanoparticle concentrations [1,2]. However, the addition of nanoparticles also increases the fluid viscosity, fluid density and the power required to pump the fluid. When the benefit of the increased heat transfer is larger than the penalty of the increased pumping power, nanofluids increase the energy efficiency of convective heat transfer.

Section 2 presents a review on Paper I which focuses on the convective heat transfer properties of nanofluids. An extensive experimental effort is undertaken to clarify some of the outstanding open issues in nanofluid based convective heat transfer. There exist discrepancies between different experiments in this field. One reason for this might be the inaccurate characterization of the microscopic and rheological properties of the studied nanofluids. The increased viscosity and pressure losses are typically studied inadequately although they directly influence the usefulness of the nanofluids in applications. In this study, turbulent convective heat transfer and pressure drop of several water-based Al_2O_3 -, SiO_2 - and MgO -nanofluids with a nanoparticle volume fraction up to 4.0 % are studied experimentally. The size distributions and shapes of nanoparticles are determined by using a combination of Dynamic Light Scattering and Transmission Electron Microscopy techniques. In addition, the various physical factors involved in heat transfer are carefully considered.

Oxygen-enriched air has applications that include combustion enhancement and emission control, fuel cell processes, medical applications, and underwater breathing. Traditional production methods are cryogenic distillation and pressure swing adsorption, which are highly energy-intensive [3,4]. Alternatively, high-purity nitrogen and oxygen-enriched air can be produced using polymeric membrane modules. By optimizing the module, flow configuration and feed parameters, the energy requirements for membrane air separation can be diminished.

Section 3 is devoted to Paper II, where the energy efficiency of the separation of air into an oxygen-enriched permeate and an oxygen-depleted residue stream in a polymeric hollow fiber membrane module is studied. A model is developed to simulate the separation of gases in counter-current lumen-feed flow, which is the most efficient flow pattern in polymeric non-porous hollow fiber membrane modules. Three system configurations are investigated in the case of air separation and compared: pressurized feed, pressurized feed with energy recovery (by means of a pneumatic motor), and vacuum mode, where a vacuum is maintained on the permeate side of the membrane. Both single-stage and two-stage processes are considered. The air separation process feed parameters (pressure ratio ϕ and stage cut θ) are optimized to minimize the specific energy consumption e of each system. The results are compared to cryogenic distillation, pressure-swing adsorption, and ion transfer membranes when oxygen-enriched air is produced. The influences of the system configuration, membrane properties, and module geometry are investigated.

Phase change materials have influenced the development of heat storage systems. Supercooling is problematic in conventional applications since it prevents the release of the stored latent heat. On the other hand, supercooling presents an opportunity for long-term heat storage when the supercooled liquid is kept at ambient temperature. The latent heat can be stored without losses for extended periods of time and released on demand by initiating the crystallization of the supercooled material.

In Section 4, Paper III is reviewed where the focus is on long-term heat storage using supercooled xylitol and specifically the crystallization of the liquid xylitol. The discharge of the stored latent heat can be started at will in temperatures below the crystallization temperature, where the liquid is at supercooled, metastable state. Xylitol has promising supercooling properties but its crystallization speed is extremely low leading to a low release rate of latent heat and to high irreversibilities in the solidification-melting process [5,6]. Several additives are experimentally studied with the objective of increasing the speed of crystallization by reducing the interfacial tension between solid and liquid phases at the crystallization front and by reducing the viscosity of the liquid phase.

2. Experimental study of turbulent convective heat transfer and pressure drop of water based oxide nanofluids inside a circular tube

A nanofluid is a suspension of ultrafine particles (<100 nm) in a conventional base fluid. Nanofluids have unique transport properties that differ from conventional suspensions. They possess better stability, a much higher specific surface area and they significantly enhance the thermal properties of conventional heat transfer fluids. Experimentally studied water based metal oxide nanofluids have enhanced heat transfer characteristics even with a low volume fraction of the nanoparticle. Several factors affect the thermal conductivity and convective heat transfer of nanofluids, and several reviews have been published [1,2,7].

The published experimental research on nanofluids has mainly focused on their thermal properties. Nanofluids exhibit enhanced thermal conductivity compared to their base fluid which cannot be explained by classical models [7]. Several articles have been published on the convective heat transfer of nanofluids; however, there exists significant discrepancies between different publications [8]. One reason for this might be the inaccurate characterization of studied nanofluids. In addition, the viscosity increase and increased pressure losses are typically studied inadequately. The influence of nanoparticles on the thermal conductivity and the mechanisms behind convective heat transfer enhancement in laminar and turbulent flow are currently not completely understood [7]. It has been shown that the increase in the thermal conductivity does not alone explain the increase in convective heat transfer coefficients [9]. It has been suggested, e.g., that the boundary layers are disrupted and that the mixing of the fluid is increased by random particle movement which leads to changes in hydrodynamic and thermal conditions [10]. According to Buongiorno [11], the convective heat transfer enhancement is the result of Brownian diffusion and thermophoresis.

In this study, water based aluminium oxide, silicon oxide and magnesium oxide nanofluids are prepared and their convective heat transfer properties are experimentally investigated. Convective heat transfer coefficients and pressure losses in turbulent flow ($Re = 3000 \dots 10000$) are measured in an experimental setup consisting of a long annular tube, where the nanofluid flows inside the inner tube and saturated steam enters the annular section creating a constant surface temperature boundary condition. The flow loop of the nanofluid contains measuring devices for temperature, pressure difference and flow rate. An ultrasonic disperser is incorporated in the flow loop to maintain the dispersion of nanoparticles. The nanofluids used in this experimental research are well characterized with respect to particle shape, particle size and particle size distribution in order to reliably identify their effects.

The objective is to establish a better understanding of nanoscale convective heat transfer phenomena by characterizing the heat transfer fluids and by determining their dynamic viscosity experimentally. The latter is of great importance, since the viscosity directly affects the Reynolds number and thus the convective heat transfer analysis. The resulting higher pressure losses in convective heat transfer are measured and analyzed. This is neglected in several studies although it directly influences the usefulness of the fluid in applications. Alternatively, heat transfer coefficients could be improved by simply increasing the flow velocity of a fluid which would require additional pumping power due to the increased pressure losses. Any attempt to enhance convective heat transfer results in increased pressure losses. Also by adding nanoparticles to the base fluid, a competition between the heat transfer augmentation and increased pressure losses is

present. Therefore, the true measure of effectiveness of a heat transfer fluid is not the convective heat transfer coefficient alone - the pressure losses need to be incorporated into the evaluation.

2.1 Characterization of nanofluids

2.1.1 Particle size distributions

Three different materials were used with distilled water as the base fluid: aluminium oxide, silicon oxide and magnesium oxide. The particle size distributions were measured with Malvern Zetasizer Nano ZS - a device based on Dynamic Light Scattering (DLS). Fig. 1 presents the average particle size distribution by number of two SiO₂ nanofluids. In several cases the measured values and the values given by the manufacturer differ, rendering the manufacturer based information unreliable. For four of the seven nanofluids, relatively narrow size distributions around a clear peak were found.

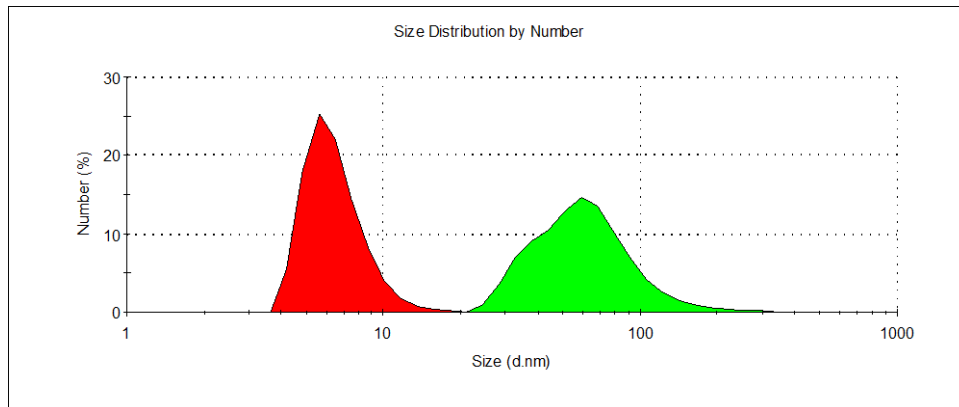


Fig. 1. Average particle size distribution by number of two SiO₂ nanofluids. *Left:* SiO₂ 6.5±1.8 nm; *right:* SiO₂ 65±34 nm.

2.1.2 Particle shapes

To determine the particle shapes, Transmission Electron Microscopy (TEM) images presented in Fig. 2 were taken from small nanofluid samples. The samples were rapidly frozen to cryogenic temperatures using a mixture of liquid ethane and propane to preserve particle configurations as accurately as possible. Three of the seven samples contained particles with irregular shapes. The measured average sizes from the DLS data are in reasonable agreement with the images.

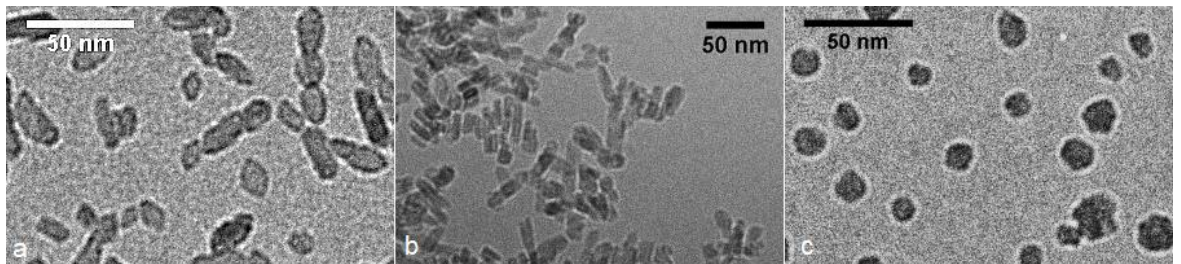


Fig. 2. Transmission Electron Microscopy images of frozen nanofluid samples at cryogenic temperatures. (a) Al₂O₃, $d_p = 8.2 \pm 3.1$ nm. (b) MgO, $d_p = 21 \pm 10$ nm. (c) SiO₂, $d_p = 6.5 \pm 1.8$ nm. Measured particle sizes are from DLS data (Table 1).

2.1.3 Viscosity measurements and physical properties

The dynamic viscosity μ of all nanofluids at all concentrations was measured using a HAAKE Falling ball viscometer C. It directly influences the results of the convective heat transfer measurements where the Reynolds number (inversely proportional to μ) is used for flow characterization.

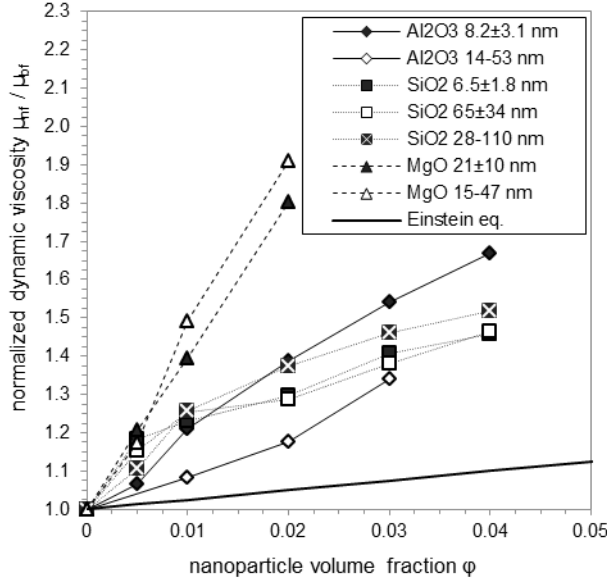


Fig. 3. Normalized dynamic viscosity μ_{nf}/μ_{bf} as a function of the nanoparticle volume fraction ϕ .

A summary of all the viscosity measurements is presented in Fig. 3. The ratio of the nanofluid viscosity to the base fluid viscosity μ_{nf}/μ_{bf} was found to be independent of temperature. As expected, the dynamic viscosity increases with increasing particle volume fraction. The measured values correspond well with pressure drop data from the heat transfer measurements. The results show that the Einstein equation, which is sometimes used in the nanofluid literature, clearly underestimates the viscosity increase in all cases.

The density ρ_{nf} of nanofluids is calculated from the well-established [12,13] equation

$$\rho_{nf} = \rho_p \phi + \rho_{bf} (1 - \phi) \quad , \quad (1)$$

where ϕ is the particle volume fraction, and ρ_p and ρ_{bf} are the particle and base fluid densities, respectively.

The specific heat capacity $c_{p,nf}$ of nanofluids is calculated from the well-established [12,13] equation

$$c_{p,nf} = \frac{\phi \rho_p c_{p,p} + (1 - \phi) \rho_{bf} c_{p,bf}}{\rho_{nf}} \quad . \quad (2)$$

2.2 Experimental setup

An experimental setup (Fig. 4) similar to that of Heris et al. [9,14] was designed and constructed in order to study the convective heat transfer characteristics of nanofluids. The heat exchanger is a 1.5 m long annular copper tube, where the nanofluid flows inside the inner tube ($d_{in} = 6.4$ mm, $d_{out} = 8.0$ mm) while subatmospheric saturated steam enters the annular section. The outer tube is well insulated. The nanofluid flow loop contains measuring devices for temperature (Pt100-type thermocouples), pressure difference (Yokogawa EJX110A differential pressure transmitter) and mass flow (KROHNE Optiflux 4000 F electromagnetic flow meter).

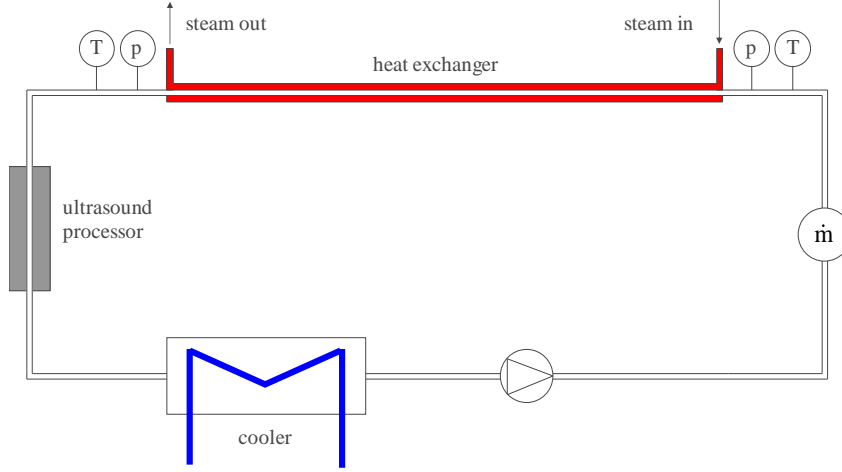


Fig. 4. A schematic diagram of the experimental setup to measure convective heat transfer and pressure losses.

2.2.1 Turbulent convective heat transfer coefficient

The turbulent heat transfer coefficient for the nanofluid flowing inside the heat exchanger tube is determined from the experimental data by first calculating the total conductance G of the heat exchanger. It is calculated from the heat transfer rate ϕ , which is the product of mass flow rate \dot{m} and temperature difference ΔT between incoming and outgoing fluid

$$G = \phi / \theta_{ln} = \dot{m} c_p \Delta T / \theta_{ln} \quad , \quad (3)$$

where θ_{ln} is the logarithmic temperature difference in the heat exchanger and c_p is the specific heat capacity of the heat transfer fluid.

The conductance per length unit G' is defined as

$$\frac{1}{G'} = \frac{1}{G/L} = \frac{1}{\pi d_{in} h} + \frac{1}{\pi d_o h_o} + \frac{\ln(d_o/d_{in})}{2\pi k_{pipe}} \quad , \quad (4)$$

where L is the length of the heat exchanger, d_{in} is the inner diameter of the test tube, h is the heat transfer coefficient for the fluid, d_o is the outer diameter of the test tube, h_o is the outer heat transfer coefficient for condensing steam, and k_{pipe} is the thermal conductivity of the pipe. The heat transfer coefficient h for fluids is solved from Eq. (4).

2.3 Convective heat transfer enhancement in turbulent flow using nanofluids

2.3.1 Heat transfer coefficients

The turbulent convective heat transfer of nanofluids is enhanced significantly over the base fluid when compared on the basis of constant Reynolds number. It can be concluded from Fig. 5 that an average increase of 46.7% in the heat transfer coefficients was found for SiO_2 nanofluids ($d_p = 28\text{--}110$ nm) when the nanoparticle volume fraction ϕ is 4%. This increase is found to be nearly independent of Re . A summary of all results is displayed in Table 1, where the average change of the nanofluid turbulent heat transfer coefficient to that of the base fluid is shown. It can be concluded that the average size of the nanoparticles, nanoparticle material and concentration have a significant influence to the heat transfer enhancement. However, quantitative dependencies on the various physical parameters are not easily found due to broad particle size distributions and due to the fact that several additional parameters affect the fluid flow and heat transfer.

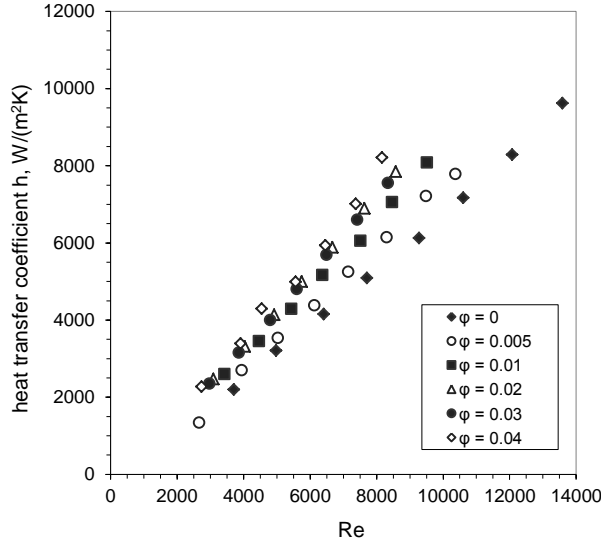


Fig. 5. Average experimental turbulent heat transfer coefficients of SiO₂ nanofluids ($d_p = 28-110$ nm) as a function of the Reynolds number.

Table 1. Summary of convective heat transfer measurements. Data show the average change in the nanofluid turbulent heat transfer coefficient as compared to the base fluid at constant Re . ($Re = 3000-10000$).

material size [nm]		nanoparticle volume fraction				
		0.005	0.01	0.02	0.03	0.04
Al ₂ O ₃	8.2±3.1	+10.5%	+28.4%	+32.5%	+40.2%	+46.3%
Al ₂ O ₃	14-53	-	+6.6%	+15.3%	+33.5%	-
MgO	21±10	+9.9%	+24.6%	+55.6%	-	-
MgO	15-47	-2.8%	+6.3%	+24.9%	-	-
SiO ₂	6.5±1.8	+26.8%	+30.1%	+34.4%	+43.1%	+43.3%
SiO ₂	65±34	+15.5%	+23.3%	+23.0%	+23.7%	+26.4%
SiO ₂	28-110	+10.4%	+28.2%	+32.6%	+35.1%	+46.7%

It is concluded that in general smaller particle size is more beneficial for heat transfer enhancement. For each particle material the nanofluid with the smallest particles has the highest heat transfer coefficients. The effect of the size is most notable when the particle concentration is low. For example, an Al₂O₃ nanofluid ($d_p = 8.2\pm 3.1$ nm) enhances heat transfer coefficients by 28.4% when the nanoparticle volume fraction $\phi = 1\%$, and a SiO₂ nanofluid ($d_p = 6.5\pm 1.8$ nm) by 26.8% when $\phi = 0.5\%$.

The results for nearly equal size Al₂O₃ and SiO₂ nanofluids ($d_p = 8.2\pm 3.1$ nm and $d_p = 6.5\pm 1.8$ nm, respectively) are very similar with the exception of the smallest volume fraction of 0.5%. Also, equal size Al₂O₃ and MgO nanofluids ($d_p = 14-53$ nm and $d_p = 15-47$ nm, respectively) show very similar heat transfer enhancement at equal volume fractions. The largest improvement was measured with a MgO nanofluid ($d_p = 21\pm 10$ nm) with a volume fraction of 2%.

The increase of the heat transfer coefficients is comparable to results presented by Kim et. al [15] and Vajjha et. al [16] despite the differences in the experimental setups and base fluids.

2.3.2 Pressure losses

Just as any other attempt to enhance convective heat transfer, adding nanoparticles to the base fluid increases pressure losses. The pressure drop Δp in a horizontal pipe based on the Blasius equation for smooth pipes in turbulent flow ($Re < 20000$) is given by White [17]:

$$\Delta p = 0.158 L \rho^{3/4} \mu^{1/4} d_{in}^{-5/4} u^{7/4} \quad (5)$$

For a smooth pipe, the pressure losses are strongly dependent on fluid density and weakly dependent on fluid viscosity. For nanofluids, both are increased with increased nanoparticle concentration leading to higher pressure losses. Furthermore, at constant volumetric flow rate the Reynolds number diminishes with increasing nanofluid particle concentration. This means that at constant Re the pressure losses are increased substantially as compared to the base fluid. In Fig. 6 the measured pressure losses of SiO_2 nanofluids (base fluid distilled water, $d_p = 28\text{-}110$ nm) inside the heat exchanger pipe are presented.

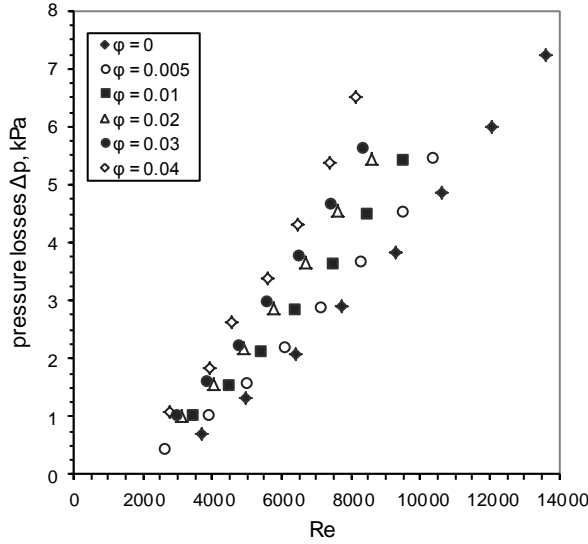


Fig. 6. Experimentally measured pressure losses of SiO_2 nanofluids (base fluid distilled water, $d_p = 28\text{-}110$ nm) as a function of the Reynolds number.

2.3.3 Efficiency of convective heat transfer

While examining only heat transfer coefficients gives very encouraging results, it does not alone reveal the true measure of effectiveness of nanofluids. Increased pressure losses directly increase the pumping power P , which in most applications is an important factor. Ideally, it is defined as

$$P = \dot{V} \Delta p \quad , \quad (6)$$

where \dot{V} is the volumetric flow rate of the heat transfer fluid.

The crucial issue to be investigated is whether or not adding nanoparticles to the base fluid is more efficient than simply increasing the flow rate of the base fluid. The relation between heat transfer enhancement and increased pumping power can be quantified by defining the so-called efficiency of convective heat transfer

$$\eta = \frac{\phi_{nf} / P_{nf}}{\phi_{bf} / P_{bf}} \quad , \quad (7)$$

where ϕ_{nf} and ϕ_{bf} are nanofluid and base fluid heat transfer rates, respectively, and P_{nf} and P_{bf} are the pumping powers of nanofluid and base fluid, respectively.

Heat transfer and pressure difference measurements are exploited to determine the convective heat transfer efficiency η is at constant volumetric flow rate for both nanofluid and base fluid. The results presented in Fig. 7 are average results in the whole measuring range. According to the results only SiO₂ nanofluids show a noticeable increase in convective heat transfer efficiency compared to the base fluid in addition to increasing the heat transfer coefficients. On the other hand, MgO nanofluids show almost exclusively values below unity.

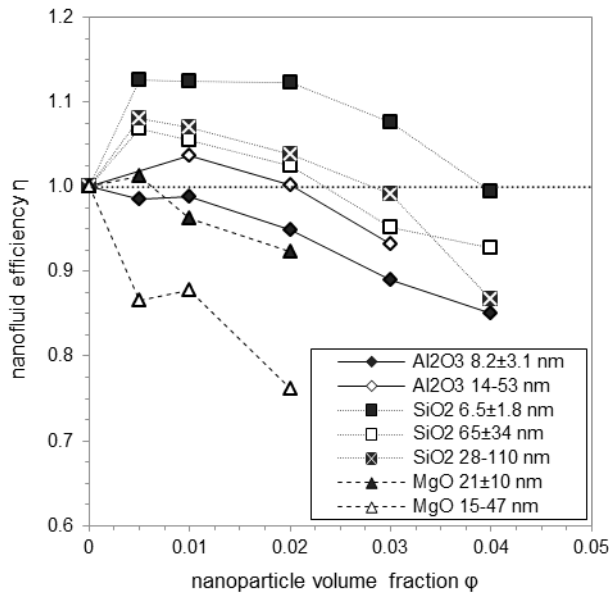


Fig. 7. Convective heat transfer efficiency η of nanofluids as a function of the nanoparticle volume fraction ϕ .

Based on our nanoparticle size and shape analysis we can conclude that small particle size is beneficial for heat transfer enhancement and low particle density, low fluid viscosity, and smooth and round particle shape are beneficial for keeping the increase of pressure losses moderate. Nearly equal size Al₂O₃ and SiO₂ nanofluids ($d_p = 8.2 \pm 3.1$ nm and $d_p = 6.5 \pm 1.8$ nm, respectively) showed similar heat transfer enhancement but when taking into account the pressure losses it is clear that the SiO₂ nanofluid is more efficient, possibly due to smooth and spherical particles. Also the density of SiO₂ particles is low compared to that of Al₂O₃ and MgO particles, which is advantageous in keeping the pressure losses moderate. Clearly SiO₂ nanofluids show the most promising results in this regard, followed by Al₂O₃ and MgO nanofluids.

The results also suggest that the convective heat transfer efficiency η is optimal when the nanoparticle concentration is low. The optimal volume fraction is in all cases between 0.5-1.0% although with the most efficient nanofluid (SiO₂, $d_p = 6.5 \pm 1.8$ nm) η is practically constant (an increase of 12.3-12.5%) between $\phi = 0.5$ -2.0%. The efficiency η decreases for all measured nanofluids when ϕ is further increased since the pressure losses increase faster than the heat transfer is enhanced. Even for the most efficient nanofluid (SiO₂, $d_p = 6.5 \pm 1.8$ nm), the convective heat transfer efficiency η drops below unity when $\phi = 4\%$.

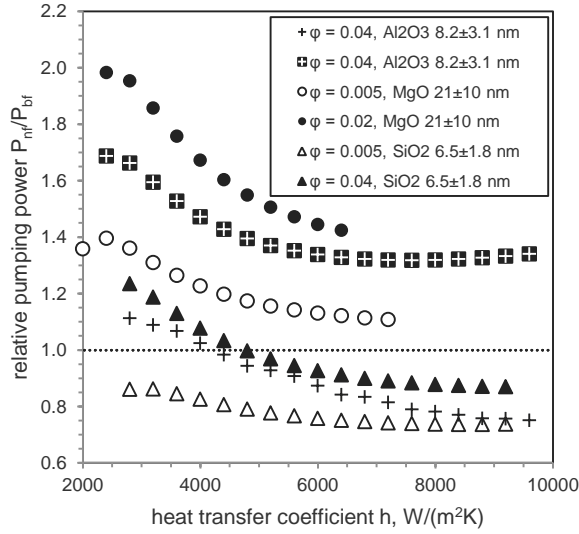


Fig. 8. Relative pumping power P_{nf}/P_{bf} of several nanofluids as a function of the heat transfer coefficient.

The effectiveness of nanofluids is further investigated by comparing the required pumping power of nanofluids and the base fluid to achieve a given heat transfer coefficient (Fig.8). This approach is less system dependent and more practical than limiting the examination to a constant volumetric flow rate. Similar to the previous results, adding small concentration of either Al_2O_3 or SiO_2 particles to the base fluid is beneficial. The relative pumping power decreases with increasing heat transfer coefficient. For the two nanofluids with the smallest nanoparticles, the pumping power can at most be decreased by approximately 25%. On the other hand, several nanofluids increase the pumping power substantially, and all the MgO nanofluids in particular. This examination confirms that increasing the nanoparticle concentration diminishes the effectiveness of nanofluids.

2.4 Conclusions

Measurements of convective heat transfer properties of water-based Al_2O_3 , SiO_2 , and MgO nanofluids with the nanoparticle volume fractions up to 4% were performed. The average convective heat transfer coefficients are enhanced in many cases by more than 40% when compared to the base fluid on the basis of a constant Reynolds number in the turbulent regime, where $Re = 3000-10000$. To understand how this enhancement depends on the microscopic properties of the nanofluids, the nanoparticles were analyzed using Dynamic Light Scattering and Transmission Electron Microscopy techniques. The main finding is that in general low density, small particle size and smooth, regular shapes are beneficial for heat transfer enhancement. For each particle phase material the nanofluid with the smallest particles has the highest heat transfer coefficient. The results also indicate that heat transfer coefficients of nanofluids increase with increasing nanoparticle concentration.

While these results confirm the claim that some nanofluids are superior to the base fluid in convective heat transfer, there are caveats in the results reported in the literature so far. In particular, the dynamic viscosity of nanofluids should be accounted for, since it directly affects the Reynolds number and thus the convective heat transfer analysis. Its significant increase together with increased density results in high pressure losses in convective heat transfer; something that has been typically inadequately considered before the present work. Here, a detailed analysis of this effect is presented. When the pressure losses are properly accounted for, only one of the nanofluids

studied here, namely the SiO₂ based nanofluid with a small concentration of smooth spherical particles (of average size 6.5 ± 1.8 nm), shows noticeable improvement in heat transfer as compared to the base fluid. It is also concluded, that increasing the nanoparticle concentration diminishes the effectiveness of all nanofluids due to increased losses. In fact, it is demonstrated that for many nanofluids the heat transfer efficiency is lower than that of the base fluid, although the bare heat transfer coefficients are larger. This shows the importance of properly characterizing the particle phase in nanofluid experiments.

3. Minimizing specific energy consumption of oxygen enrichment in polymeric hollow fiber membrane modules

A study on modeling and optimization of the separation of air into an oxygen-enriched permeate and an oxygen-depleted residue stream by polymer membranes is presented in Paper II. A counter-current lumen-feed gas separation model is developed and used to optimize various parameters in order to minimize the specific energy consumption of air separation in membrane systems. The results are used to compare membrane air separation to other existing technologies.

The driving force in membrane gas separation is the partial pressure difference across a selective membrane. Due to different permeation rates a gas mixture is enriched but rarely completely separated. A sufficient pressure difference is induced by either pressurizing the feed stream or by drawing a vacuum on the permeate side. Increasing the pressure difference increases the permeate flow through the membrane and the purity of the permeate when a gas mixture is separated.

Membrane systems are limited to the production of oxygen-enriched air. The polyimide membranes currently used in commercial air separation have O_2/N_2 selectivities of 6-7 [18,19], resulting in oxygen-enriched air rather than pure oxygen; e.g., a membrane with a selectivity of 7 can theoretically only produce 65 percent pure oxygen, when the stage cut is zero and the pressure ratio is infinite.

A model is developed to simulate the separation of gas components in counter-current lumen-feed flow in three system configurations (pressurized feed, pressurized feed with energy recovery (by means of a pneumatic motor), and vacuum mode, where a vacuum is maintained on the permeate side of the membrane). Both single-stage and two-stage processes are studied. The air separation process feed parameters (pressure ratio ϕ and stage cut θ) are optimized to minimize the specific energy consumption e of each system.

3.1 Model development

The transport model is based on mass transfer resistances in the membrane and in forming concentration boundary layers adjacent to the membrane surfaces. The influence of the concentration boundary layers (concentration polarization) is estimated with correlations presented in the literature. Sanchez and Mourgues [20] suggest that the effects of concentration polarization are noticeable when the permeation rates are high and the membrane is highly selective.

Gas transport through non-porous membrane material is described by the solution-diffusion model [21], which includes three consecutive steps. Gas molecules on the high partial pressure side dissolve into the membrane surface, diffuse through the dense membrane material, and finally desorb at the opposite surface. Each gas component permeating through the membrane has a characteristic permeability that is based on solubility S and diffusivity D in the membrane material. Selectivity α_{ij} is the ratio of permeabilities for a specific gas pair and it is a fundamental parameter describing the membrane separation capability. It is defined as

$$\alpha_{ij} = b_i / b_j = \frac{D_i S_i}{D_j S_j} . \quad (8)$$

The dimensionless stage cut parameter θ is defined as the ratio of the permeate and feed molar flow rates

$$\theta = \dot{n}_{perm} / \dot{n}_{feed} \quad . \quad (9)$$

The pressure ratio ϕ is defined as

$$\phi = p_{feed} / p_{perm} \quad . \quad (10)$$

3.1.1 Fiber model

An isothermal, steady-state process where the feed and permeate flow in opposite directions is modeled. Fig. 9 presents a schematic of the flows in a fiber section. Ideal gas behavior is assumed. The mass transfer of gas components between the lumen and shell may be expressed as

$$d\dot{m}_{i,l} = -d\dot{m}_{i,s} = -\dot{m}_i^* dA_{eff} \quad , \quad (11)$$

where the mass flux is dependent on the total mass transfer coefficient K_i and the partial pressure difference Δp_i

$$\dot{m}_i^* = \frac{K_i \Delta p_i M_i}{R_g T} \quad . \quad (12)$$

The differential effective membrane area dA_{eff} is based on the logarithmic mean diameter of the tubular membrane and is described by

$$dA_{eff} = \pi \frac{d_{out} - d_{in}}{\ln(d_{out} / d_{in})} dz \quad . \quad (13)$$

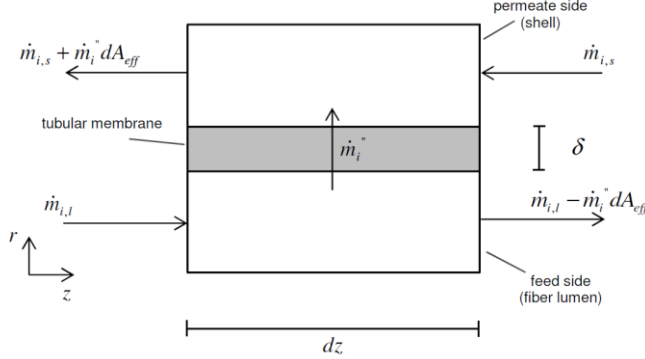


Fig. 9. Schematic representation of counter-current flows inside a hollow fiber membrane module.

The mass transfer coefficient K_i is based on mass transfer resistances in the membrane and in forming concentration boundary layers adjacent to the membrane surfaces as follows:

$$R_i = \frac{1}{K_i} = \frac{1}{k_{i,l}} + \frac{1}{k_{i,m}} + \frac{1}{k_{i,s}} \quad . \quad (14)$$

The mass transfer resistance in the fiber lumen is approximated with the well-established L ev eque correlation for laminar flow:

$$k_{i,l} = Sh_l D / d_{in} \quad (15)$$

$$Sh_l = 1.62 \left(Re Sc \frac{d_{in}}{L} \right)^{\frac{1}{3}} = 1.62 \left(\frac{d_{in}^2 v_{lumen}}{DL} \right)^{\frac{1}{3}} \quad (16)$$

A thin membrane and high permeability lead to a small mass transfer resistance. The flux through a membrane is inversely proportional to the thickness δ of the membrane:

$$k_{i,m} = b_i / \delta \quad (17)$$

Donohue's correlation (Eq. (19)) has been successfully used and validated by several authors in hollow fiber mass transfer models for gases [22-24]

$$k_{i,s} = Sh_s D / d_{out} \quad (18)$$

$$Sh_s = 0.0732 (d_h / [cm])^{0.60} Re^{0.60} Sc^{0.33} \quad , \quad (19)$$

where d_h is the hydraulic diameter defined as

$$d_h = 4A_{cs,s} / U = \frac{4 \cdot (\pi d_m^2 / 4 - N_f \pi d_{out}^2 / 4)}{\pi d_m + N_f \pi d_{out}} = \frac{d_m^2 - N_f d_{out}^2}{d_m + N_f d_{out}} \quad . \quad (20)$$

The pressure drop along the fiber length is described by the Hagen-Poiseuille equation, which assumes fully developed velocity profiles, negligible compressibility effects and a no-slip condition on the membrane surface. Inside the lumen it leads to

$$dp_l / dz = -32\mu v_l / d_{in}^2 \quad . \quad (21)$$

The axial pressure drop in the shell, i.e. in the space between the fibers of a hollow fiber membrane module is usually neglected. Since the geometry of the module is considered in this study, the pressure drop in the shell has been included in the model. It is estimated by using the hydraulic diameter concept

$$dp_s / dz = -32\mu v_s / d_h^2 \quad , \quad (22)$$

where the hydraulic diameter d_h is defined in Eq. (20).

The following boundary conditions are considered:

$$\text{for } z=0 \quad , \quad x_{O_2,l} = 0.21 \quad (23)$$

$$\text{and} \quad p_l = p_{feed} \quad (24)$$

$$\text{and} \quad \dot{m}_l = \dot{m}_{feed} \quad (25)$$

$$\text{and} \quad p_s = p_{perm} \quad (26)$$

$$\text{for } z=L \quad , \quad \dot{m}_s = 0 \quad (27)$$

$$\text{and} \quad \dot{m}_{s,O_2} = 0 \quad (28)$$

3.2 Specific energy consumption of membrane air separation

Each membrane air separation configuration consists of one or more devices that consume power. The single-stage system configurations are illustrated in Fig. 10. The isothermal power consumption of a cooled compressor P_{comp} is

$$P_{comp} = \dot{m}_{feed} R_g T \ln \phi / \eta_{comp} \quad , \quad (29)$$

where \dot{n}_{feed} is the feed molar flow and η_{comp} is the overall efficiency of the compressor.

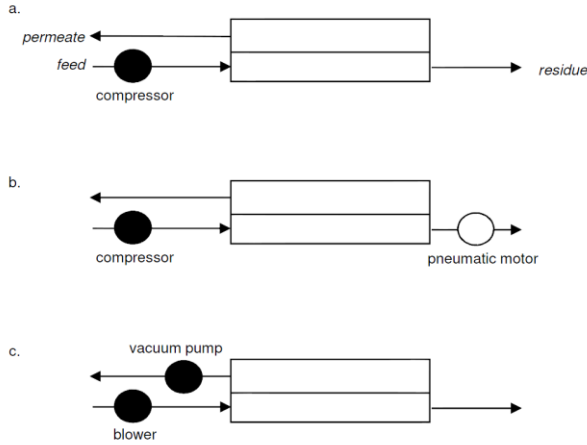


Fig. 10. Illustration of three single-stage configurations: a. pressurized feed, b. pressurized with energy recovery, c. vacuum mode.

Similarly, the isothermal power consumption of a vacuum pump P_{vac} is

$$P_{vac} = \dot{n}_{perm} R_g T \ln \phi / \eta_{vac} \quad , \quad (30)$$

where \dot{n}_{perm} is the permeate molar flow and η_{vac} is the overall efficiency of the vacuum pump.

The efficiency of a vacuum pump η_{vac} decreases with increasing vacuum quality. Eq. (31) is determined from [24] and is valid for pressures higher than 100 Pa:

$$\eta_{vac}(p_{perm}) = 0.2261 \cdot \log(p_{perm}) + 0.050 \quad . \quad (31)$$

The mechanical power recovered by a pneumatic motor P_{pne} in an isentropic process is

$$P_{pne} = \dot{m}_{res} c_p T \left(1 - (p_{res} / p_0)^{\frac{\gamma}{\gamma-1}} \right) \cdot \eta_{pne} \quad , \quad (32)$$

where \dot{m}_{res} is the residue mass flow and p_{res} is the residue pressure. The ratio of specific heats γ for oxygen-depleted air is 1.4. p_0 is the atmospheric pressure and η_{pne} is the isentropic efficiency of the pneumatic motor. The values used for η_{comp} and η_{pne} are both 0.75.

If a pressurized feed is used, a pneumatic motor together with a generator can be used to convert energy from the high- pressure residue stream into electricity, thus increasing the efficiency of the separation process. In vacuum mode one blower is required to generate the feed stream at essentially atmospheric pressure while the vacuum pump is used to generate a vacuum on the permeate side. The power consumption P of each system is

$$\text{a:} \quad P = P_{comp} \quad (33)$$

$$\text{b:} \quad P = P_{comp} - \eta_g P_{pne} \quad (34)$$

$$\text{c:} \quad P = P_{comp} + P_{vac} \quad (35)$$

The specific energy consumption e (kJ/mol(O₂)) of each system is defined as

$$e = P / \dot{n}_{perm,O_2} \quad (36)$$

where \dot{n}_{perm,O_2} is the permeate molar flow of oxygen.

3.3 Results and discussion

3.3.1 Effects of selectivity α , pressure ratio ϕ , and stage cut θ on oxygen enrichment

Fig. 11 demonstrates the effect of stage cut θ , pressure ratio ϕ , and membrane selectivity α on oxygen enrichment in counter-current lumen-feed. It is not possible to achieve both high enrichment and a high stage cut simultaneously. At low feed rates (high stage cut) the feed side concentration of the more permeable gas diminishes along the membrane length, resulting in a lower driving force and a lower enrichment. A high feed rate (low stage cut) leads only to minor changes in the feed side concentrations and to a higher enrichment. A very low stage cut is achieved when the feed rate is very high. This leads to a high pressure drop in the fiber lumen, resulting in a diminished driving force and less effective separation.

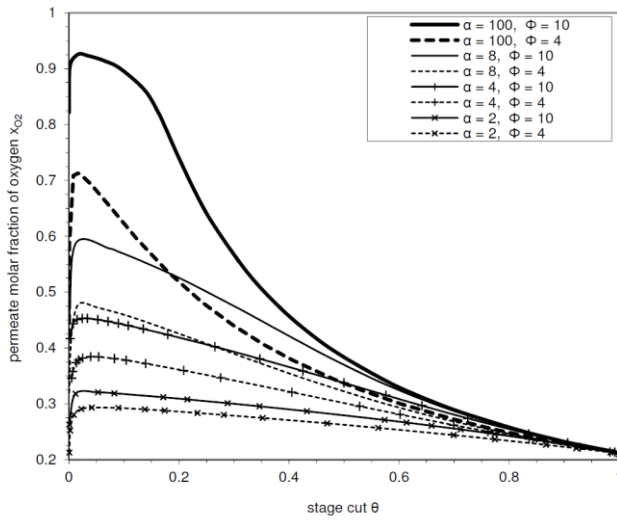


Fig. 11. Effects of selectivity α , pressure ratio ϕ , and stage cut θ on oxygen enrichment in vacuum mode.

3.3.2 Influence of flow parameters on the specific energy consumption e

Fig. 12 presents a typical result when using a pressurized feed with a 21% molar fraction of oxygen to produce oxygen-enriched air with a 30% molar fraction of oxygen. Also results for the same case are shown when the driving force is created by a vacuum on the permeate side. In general the specific energy consumption e is considerably lower since the subatmospheric pressure has to be applied only to the fraction that penetrates the membrane. Optimal values for the specific energy consumption e are found for different permeate purities. The results illustrate that the correct choice of feed parameters is of importance to energy efficiency, especially when the required molar fraction of oxygen is low.

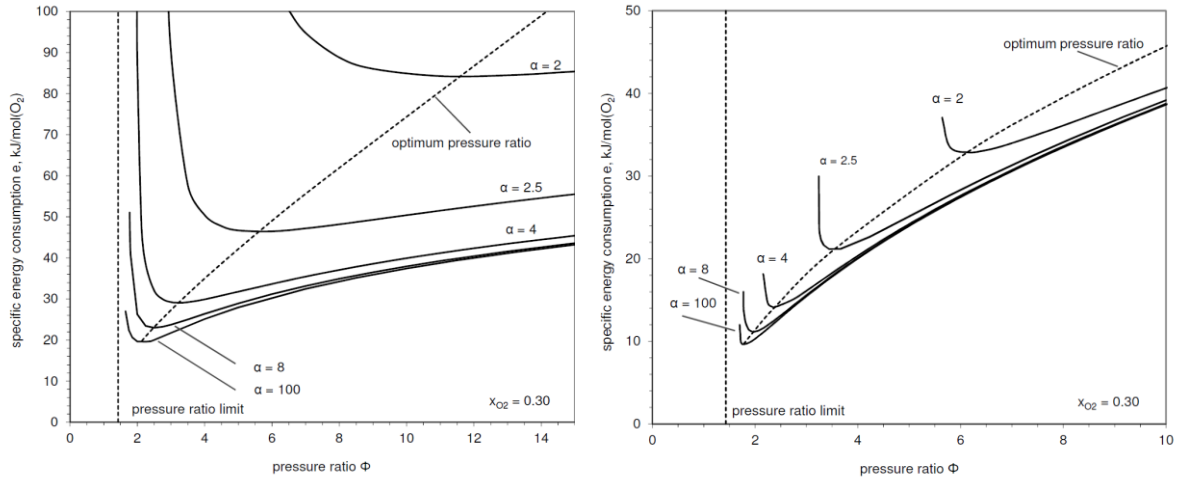


Fig. 12. Effects of pressure ratio ϕ and selectivity α on the specific energy consumption e when the molar fraction of oxygen in the permeate is $x_{O_2} = 0.30$. *Left*: pressurized feed. *Right*: vacuum mode.

3.3.3 Influence of the module geometry on the specific energy consumption e

The geometry parameters must be chosen correctly to avoid a negative impact on the efficiency of the separation process; e.g., the inner diameter of the fiber lumen should be greater than 100 μm in order to avoid excessive pressure drops. Very long fibers and fully packed modules result in pressure losses in the lumen and in the shell of the fiber, respectively, increasing the specific energy consumption of the separation process. The optimization of the feed parameters is more important than the optimization of the module geometry. Perhaps non-intuitively, decreasing the membrane thickness decreases energy efficiency due to an increased influence of concentration polarization and higher pressure losses.

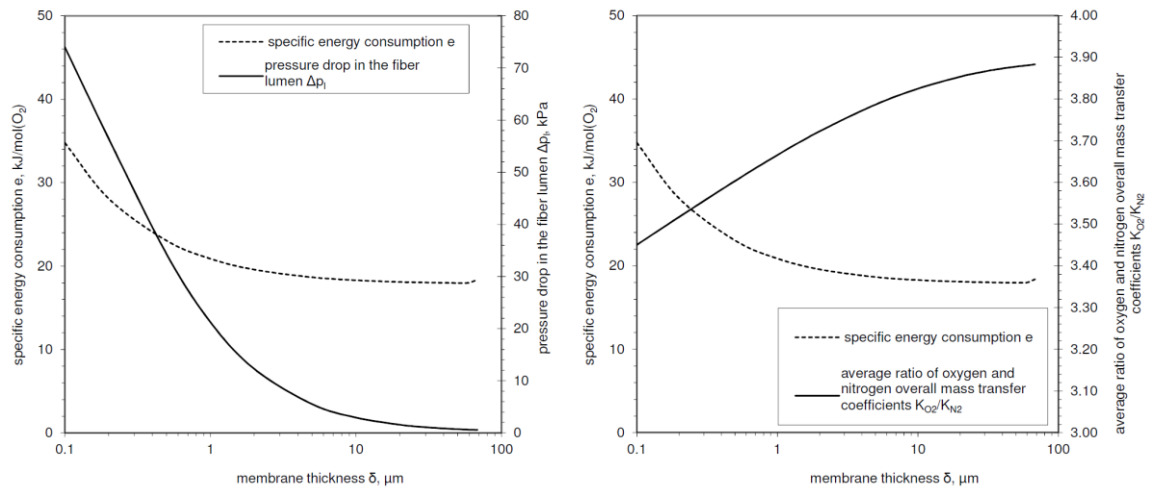


Fig. 13. Influence of the membrane thickness δ on the specific energy consumption e , the pressure drop in the fiber lumen Δp_l (*left*), and on the average ratio of oxygen and nitrogen overall mass transfer coefficients K_{O_2}/K_{N_2} (*right*) in vacuum mode when $\alpha = 4$ and $x_{O_2} = 0.35$. Stage cut θ and pressure ratio Φ are optimized separately at each point. The increase in the specific energy consumption is partly caused by the higher pressure drop and partly by the increased influence of concentration polarization.

The simulation results reveal that if the membrane thickness is below 5 μm , while all other geometry parameters are kept constant, the energy efficiency is decreased (Fig. 13). This result might at first look contradictory to many efforts to minimize membrane thickness in order to improve productivity. Firstly, a thinner membrane leads to a higher permeate flow but at the same

time the feed flow has to be increased substantially to maintain the desired oxygen enrichment. A higher feed flow leads to a higher pressure drop and to a decrease in the driving force (a lower driving force lowers the oxygen enrichment) which must be compensated by increasing the pressure ratio or the feed flow rate. Secondly, the influence of the concentration boundary layers is increased when the membrane is thinner. The ratio of the oxygen and nitrogen average overall mass transfer coefficients is decreased due to the increased influence of concentration polarization. In order to maintain the desired oxygen enrichment, the optimal specific energy consumption is slightly higher compared to a thicker membrane.

3.3.4 Comparison of system configurations

In Fig. 14 the three system configurations presented in Section 3.2 are compared. The vacuum mode is by far the most energy-efficient. The main reason for this is that only the fraction that permeates the membrane passes through the vacuum pump. A two-stage process can be advantageous if the energy efficiency of the separation is considered. When both modules and feed parameters in both stages are optimized, the specific energy consumption of the two-stage process is in many cases favorable compared to that of a single-stage process (Fig. 14). In addition, using two modules in series permits a higher enrichment of oxygen. The disadvantage of this system configuration is that a smaller fraction of the feed is recovered and that the membrane area in relation to the gas produced is increased. This increase diminishes the cost-efficiency of the two-stage process, but this kind of evaluation lies beyond the scope of this study.

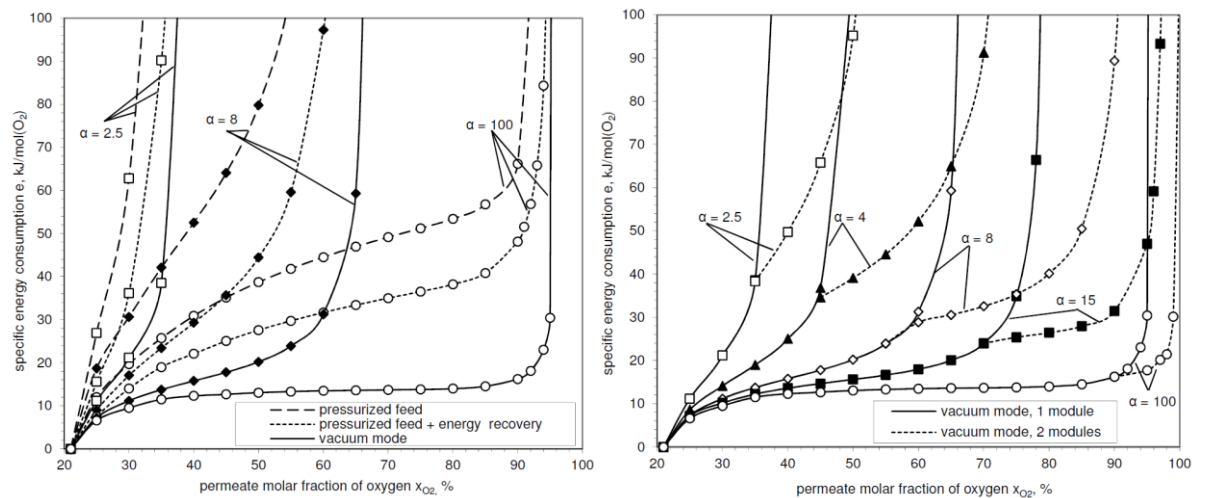


Fig. 14. *Left:* Comparison of three system configurations. The optimized specific energy consumption e is presented as a function of the molar fraction of oxygen in the permeate x_{O_2} . *Right:* The optimized specific energy consumption e of membrane air separation in vacuum mode with one module and with two modules in series as a function of x_{O_2} .

When the desired molar fraction of oxygen is 50%, a membrane module with a selectivity of 8 can compete with even large-scale cryogenic distillation and ion transfer membranes if the process is optimized (Fig. 15). On the other hand, membrane separation is clearly more energy-efficient when compared to small-scale cryogenic distillation and pressure swing adsorption. As a result, polymer membranes are most suitable in small applications where the desired oxygen purity is fairly low. A membrane with a selectivity of 100 would be more efficient than other techniques up to an oxygen purity of approximately 92%.

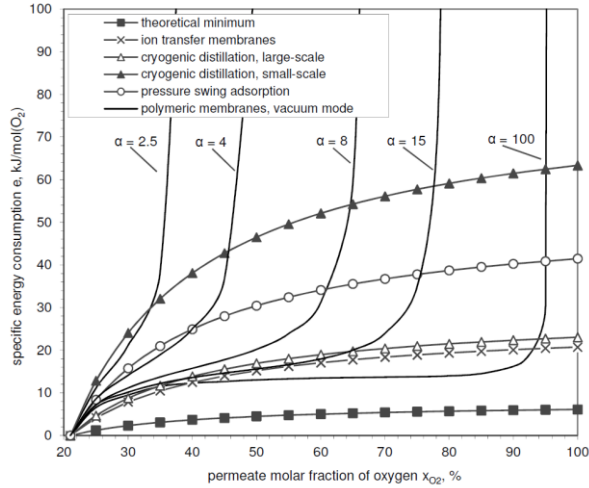


Fig. 15. The optimized specific energy consumption e of membrane air separation in vacuum mode compared to other techniques.

3.4 Conclusions

The modeling and optimization of air separation by polymer membranes has been presented in this study. A counter-current lumen-feed gas separation model was presented and used to optimize various parameters in order to minimize the specific energy consumption of air separation in membrane systems. The important geometry parameters and feed parameters were recognized.

The higher the selectivity of a membrane, the more important the choice of the feed parameters (pressure ratio and stage cut) becomes. This is also true when the desired oxygen content is low since only a small deviation from the optimal feed parameters results in a significant decrease in energy efficiency.

The geometry parameters must be chosen correctly to avoid a negative impact on the efficiency of the separation process; e.g., the inner diameter of the fiber lumen should be greater than 100 μm in order to avoid excessive pressure drops. Very long fibers and fully packed modules result in pressure losses in the lumen and in the shell of the fiber, respectively, increasing the specific energy consumption of the separation process. Perhaps non-intuitively, decreasing the membrane thickness decreases energy efficiency due to an increased influence of concentration polarization and higher pressure losses. On the other hand, the optimization of the feed parameters is more important than the optimization of the module geometry.

The vacuum mode, where a vacuum is maintained on the permeate side of the membrane, was found to be distinctly more efficient than the pressurized feed configuration. This is the case even if energy is recovered from the high-pressure residue by means of a pneumatic motor.

A two-stage process can be advantageous if the energy efficiency of the separation is considered. When both modules and feed parameters in both stages are optimized, the specific energy consumption of the two-stage process is in many cases favorable compared to that of a single-stage process. In addition, using two modules in series permits a higher enrichment of oxygen. The disadvantage of this system configuration is that a smaller fraction of the feed is recovered and that the membrane area in relation to the gas produced is increased. This increase diminishes the cost-efficiency of the two-stage process, but this kind of evaluation lies beyond the scope of this study.

If the air separation is optimized in order to minimize the specific energy consumption, membranes can compete with other more established technologies to produce oxygen-enriched air. On the other hand, choosing the feed parameters poorly will increase the specific energy consumption dramatically. Present-day membranes are most suitable in small applications where the desired oxygen purity is fairly low. If the desired molar fraction of oxygen is 50%, an optimized membrane module with a selectivity above 8 can compete with even large-scale cryogenic distillation and ion transfer membranes. A polymeric membrane with a selectivity of 100 would be more efficient than other techniques up to an oxygen purity of approximately 92%.

4. Improving the heat discharge rate of a thermal storage based on supercooled xylitol

Supercooled phase change materials can be used in special long-term heat storage applications. The discharge of the stored latent heat can be started at will in cold temperatures (temperatures below the crystallization temperature). Xylitol ($C_5H_{12}O_5$, (2S,4R)-pentane-1,2,3,4,5-pentol) is a sugar alcohol used as a sugar substitute and in pharmaceuticals. Its high specific latent heat and non-corrosiveness make it a candidate for long-term heat storage material. Furthermore, xylitol can be easily supercooled to room temperature and below (the melting temperature of pure xylitol is about 92 °C). However, the speed of crystallization is low leading to a low release rate of the stored latent heat.

Based on the classical nucleation theory [25], the nucleation rate can be increased by decreasing the activation energy E and by decreasing energy barrier ΔG , which is required to form the critical nucleus. It is often assumed that E is closely related to the activation energy of the transport coefficients such as viscosity and diffusivity, while ΔG depends on the interfacial energy γ and the Gibbs free energy difference ΔG_v between the two bulk phases

$$\Delta G \propto \gamma^3 / \Delta G_v^2 . \quad (37)$$

Several additives (including alcohols and salt hydrates) are used in experiments with the objective of increasing the speed of the crystallization front of xylitol by reducing the interfacial tension between solid and liquid phases at the crystallization front and the viscosity of the liquid phase.

4.1 Experimental methods

Industrial quality xylitol crystal samples (mass 2 g) together with the additives were placed inside sealed glass test tubes. The melted samples were then cooled and supercooled in a constant temperature water bath. The crystallization was initialized by placing some seed crystals onto the surface of the melted mixture. The speed of the advancing crystallization front was then measured over a period of 1–50 h. In those experiments where the position of the crystallization front has become fragmented, the advancing crystallization front and crystal growth rate were determined from video images. Here, no uniform phase boundary exists and the progress of the crystallization proceeds more or less randomly. For such cases, the mean value and the standard deviation of 5–10 repeated experiments are presented. Flow currents were detected by a microscope. A Differential Scanning Calorimeter was used to determine that additives did not significantly affect the melting temperature or the heat of melting.

4.2 Results

4.2.1 Propagation of the crystallization front at room temperature

The samples were cooled to a temperature of 22 °C without crystallization, corresponding to 70 °C supercooling for pure xylitol. The additives ethanol and acetone occasionally caused premature crystallization. The speed of the crystallization front of a pure xylitol was found to be 0.7 ± 0.1 mm/h. All tested additives with the exception of rapeseed oil increased the crystallization speed (Table 2). E.g. adding 5 w-% of water increases the speed to 6.0 ± 0.3 mm/h. The highest speeds, about 10 times greater than for pure xylitol, were found for acetone, ethanol and methanol. A small amount of surfactant (sodium dodecyl sulphate) further improves the speed by 20% when 5 w-% ethanol is the main additive. However, the speed decreases, if SDS is combined with methanol, acetone or water.

Table 2. Propagation velocity of the crystallization front with different additives in room temperature. Concentration of additives 5 w-% unless differently stated.

additive	velocity, mm/h
none (pure xylitol)	0.7 ± 0.1
rapeseed oil	0.2 ± 0.03
sodium acetate trihydrate	1.6 ± 0.1
glycerol	2.2 ± 0.3
phosphoric acid	2.2 ± 0.4
ethylene glycol	2.8 ± 0.3
sodium bicarbonate [2 w-%, 5 w-%] + H ₂ O [5 w-%]	4.0 ± 0.3
sodium carbonate [2 w-%, 5 w-%] + H ₂ O [5 w-%]	4.1 ± 0.4
K-acetate [2 w-%] + H ₂ O [5 w-%]	4.5 ± 0.3
ethyl acetate	4.9 ± 0.4
1-Decanol	5.0 ± 0.5
acetic acid monohydrate	5.2 ± 0.3
Citric acid [2 w-%, 5 w-%] + H ₂ O [5 w-%]	5.4 ± 0.3
K-citrate [2 w-%, 5 w-%] + H ₂ O [5 w-%]	5.4 ± 0.4
ammonium chloride	5.4 ± 0.4
Mg-acetate tetrahydrate [2 w-%] + H ₂ O [5 w-%]	5.5 ± 0.3
K-phosphate [2 w-%] + H ₂ O [5 w-%]	5.8 ± 0.3
Mg-sulphate heptahydrate	6.0 ± 0.5
Water	6.0 ± 0.3
1-Dodecanol	6.0 ± 0.5
1-Octanol	6.1 ± 0.5
Methanol	7.3 ± 0.4
Acetone	7.3 ± 0.4
Ethanol	7.3 ± 0.4

4.2.2 Methanol as an additive

With methanol, an interesting phenomenon occurs when its concentration is higher than 5%. Crystallized particles or layers are spontaneously loosened and they settle a few millimetres lower than the main solidification zone (Fig. 16). These new nucleation centers accelerate the solidification and the release of latent heat (Fig.17). Other additives did not show this kind of behavior. In the vertical experiments with a methanol content of 15%, the speed of the crystallization front was about 33 times faster than the speed of pure xylitol.

In a small glass tube ($d = 2.5$ mm) the speed of the crystallization front of pure xylitol in horizontal and vertical experiments is equal. However, in a horizontal larger tube ($d = 8$ mm) with a gas layer above the xylitol the results for horizontal showed a six time increase. If methanol is added, small loose crystallized particles can be found several centimeters ahead of the main crystallization zone, speeding up the crystallization more effectively than in the vertical experiments, where the loose layers settled only a few millimeters ahead of the main interface. Compared to pure xylitol the crystallization front velocities were up to 33 times higher in vertical experiments and up to 170 times higher in horizontal experiments.

The improved speed of crystallization is mostly caused by methanol flow currents that result from the separation of methanol during crystallization, and to a lesser extent, as a result of the increased crystal growth speed. Small detached crystallized particles are transported by the currents to the non-crystallized fluid, initiating crystallization outside the main crystallization zone. The microflows can be observed only by microscope. In vertical experiments the effect is less profound since low density methanol currents in the direction of the non-crystallized high density xylitol are hindered by the buoyant force.

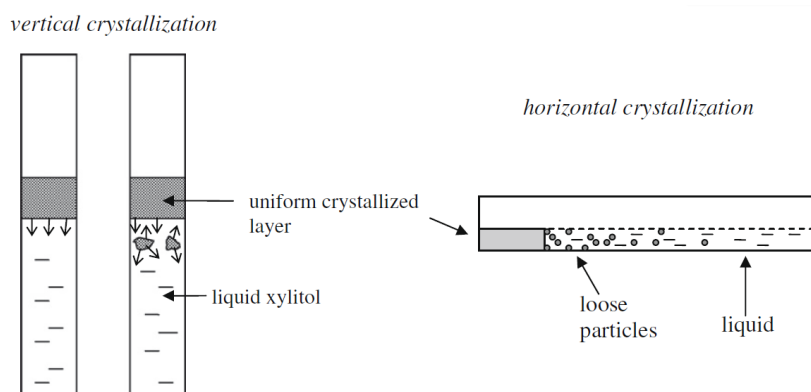


Fig. 16. The movement of the crystallization front inside the test tubes. Arrows describe the direction of crystallization. *Left*: the crystallized front moves uniformly downwards in a vertical experiment. *Middle*: crystallized particles or layers come loose from the main crystallization zone and settle at a lower level, accelerating the crystallization process. *Right*: in a horizontal experiment small crystallized particles may float for a longer distance than in vertical experiments.

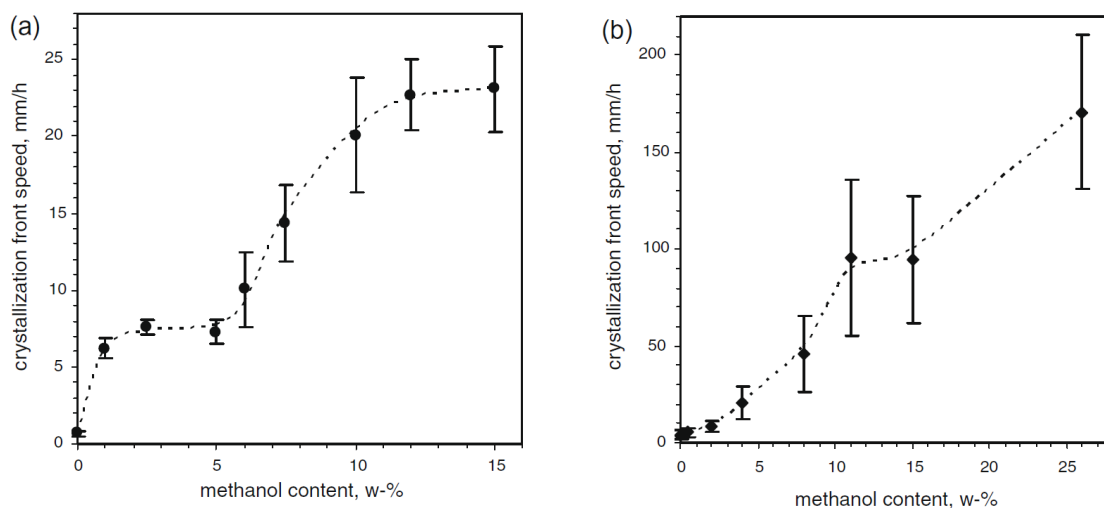


Fig. 17. The effect of the concentration of methanol on the speed of the crystallization front of xylitol in: (a) vertical experiments; (b) horizontal experiments with a gas layer above the solidifying xylitol. The points correspond to the average and the vertical bars to the standard deviation of multiple tests.

4.2.3 The effect of temperature on the speed of the crystallization front

At temperatures below room temperature, where the degree of supercooling is further increased, the propagation of the crystallization front is slowed down (Fig. 18). Still, the additives increase the crystallization speed. Each mixture has its own temperature and degree of supercooling where the speed reaches a maximum value. If the temperature rises above 75 °C, all of the studied additives diminish the speed.

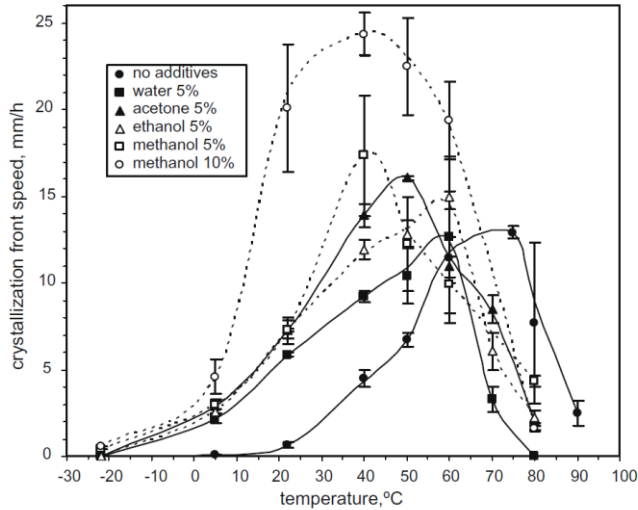


Fig. 18. The speed of the crystallization front with various temperatures. The points correspond to the average and the vertical bars to the standard deviation of multiple tests.

4.2.4 Long-term durability in supercooled state

Indicative results about the long-term supercooling ability of xylitol were obtained by placing xylitol samples inside a sealed glass test tube in room temperature. Small samples (2 g) of liquid xylitol at room temperature have avoided crystallization for four years. The ability of liquids to supercool decreases with increasing volume [26]. When the sample size is increased to 200 g, test samples of pure xylitol crystallized spontaneously after two months. With added methanol (5 w-%) a sample crystallized spontaneously after one week.

4.3 Conclusions

Based on the results, acetone and alcohols such as ethanol and methanol are the best additives for the purpose of increasing the crystallization velocity of supercooled xylitol. With methanol, up to 170 times faster velocities were measured. On the other hand, even adding water clearly speeds up the crystallization. Further improvements are certainly possible by exploiting even more suitable additives and combining them appropriately. The latent heat and the melting temperature of xylitol were not affected by the additives. Although the tested additives substantially improved the speed of the crystallization front, the speed is still very low compared to many other substances. Further improvement in the speed of crystallization is needed if xylitol is to be used as an energy efficient heat storage.

5 Summary

5.1 Main results

Three separate studies concerning the efficiency of energy related processes were reviewed. Firstly, convective heat transfer properties of water-based Al_2O_3 , SiO_2 , and MgO nanofluids 4% were measured and analyzed. Average convective heat transfer coefficients are significantly enhanced when compared to the base fluid on the basis of constant Reynolds number. An increase of over 40 % was observed for several nanofluids. The main finding is that in general low density, small particle size and smooth, regular shapes are beneficial for heat transfer enhancement. For each particle phase material the nanofluid with the smallest particles has the highest heat transfer coefficients. The significant increase of the dynamic viscosity together with increased density results in high pressure losses in convective heat transfer; something that has been typically inadequately considered before the present work. When the pressure losses are properly accounted for, only one of the nanofluids studied here, namely the SiO_2 based nanofluid with a small concentration of smooth spherical particles (of average size 6.5 ± 1.8 nm), shows noticeable improvement in convective heat transfer as compared to the base fluid. It is also concluded, that increasing the nanoparticle concentration diminishes the effectiveness of all nanofluids due to increased losses. In fact, it is demonstrated that for many nanofluids the heat transfer efficiency is lower than that of the base fluid, although the heat transfer coefficients are significantly larger.

Secondly, a model of gas separation in hollow fiber membrane modules is presented and used to simulate counter-current lumen-feed air separation. Various parameters are optimized in order to minimize the specific energy consumption of the separation. The important geometry parameters and feed parameters were recognized. The vacuum mode, where a vacuum is maintained on the permeate side of the membrane, was found to be distinctly more efficient than the pressurized feed configuration. This is the case even if energy is recovered from the high-pressure residue by means of a pneumatic motor. A two-stage configuration, where the permeate of the first module is further enriched in a second stage, is also considered. By optimizing both stages the specific energy consumption can, in some cases, be further reduced. The optimization of the module geometry is not as important as the optimization of the feed parameters – the pressure ratio and stage cut. If the separation is optimized in order to minimize the specific energy consumption, membranes can compete with other more established technologies to produce oxygen-enriched air. On the other hand, choosing the feed parameters poorly will increase the specific energy consumption dramatically. Present-day membranes are most suitable in small applications where the desired oxygen purity is fairly low. If the desired molar fraction of oxygen is 50%, an optimized membrane module with a selectivity above 8 can compete with even large-scale cryogenic distillation and ion transfer membranes.

Thirdly, increasing the crystallization speed of supercooled xylitol with the use of additives was studied. Supercooled phase change materials can be used in special long-term heat storage applications. The discharge of the stored latent heat can be started at will in temperatures below the crystallization temperature. The results show that acetone, ethanol and methanol are the most efficient substances for this purpose. The latent heat and the melting temperature of xylitol were not affected by the additives. With a sufficiently large percentage of methanol, crystallized particles or layers are spontaneously loosened. These new seed crystals accelerate the solidification and the release of latent heat. Up to 170 times faster velocities were measured compared to pure xylitol. Still, this is as much as four magnitudes lower than the crystallization speed of supercooled water. Furthermore, indicative results suggest that additives increase the likelihood of spontaneous

crystallization. Further improvements are needed and certainly possible by exploiting even more suitable additives and combining them appropriately.

5.2 Discussion and future outlook

Nanofluids have been considered for applications as advanced heat transfer fluids, since they provide enhanced thermal properties and have better suspension stability compared to micron-sized solid particles. The low thermal conductivity of conventional fluids is improved when solid particles with significantly higher thermal conductivity are added. It has been shown that for nanofluids the increase in thermal conductivity alone cannot explain the anomalous convective heat transfer enhancement. The increased viscosity of nanofluids compared to base fluid increases the power required to pump the fluid through a system. When the benefit of the increased heat transfer is larger than the penalty of the increased pumping power, nanofluids have the potential for commercial viability.

In this study, the potential of nanofluids as heat transfer fluids is confirmed, as the pumping power required to drive the fluid flow can be decreased by as much as 25% with suitable nanoparticles. All nanofluid properties are dependent on several parameters including nanoparticle material, concentration, size, and shape – parameters that can be adjusted and optimized. In general nanofluids show many promising properties for heat transfer applications. A nanofluid that meets all requirements (enhanced heat transfer coefficients, long-term stability and low viscosity) has not been proposed yet.

The field of nanofluid research has rapidly become an exciting topic in heat transfer and nanoscience research. Nanofluids have great potential to impact convective heat transfer in a way that no other known materials can. A great advantage is that nanofluids can be used to replace the existing heat transfer fluids without any modification to the actual heat exchangers.

Air separation using polymeric materials is based on the difference in permeabilities of oxygen and nitrogen through a membrane which separates high-pressure and low-pressure streams. The pressure ratio and membrane selectivity determine the separation limits. Membrane systems are limited to the production of oxygen enriched air. A major benefit of membrane separation is the simple, continuous nature of the process and operation at near ambient conditions. The optimization of the feed parameters greatly influences the energy efficiency of the separation process. Although it is shown in this study that the specific energy consumption is comparable to traditional production techniques and although polymeric membranes and membrane processes will keep improving, it is expected that cryogenics will remain the main process for large scale production of high purity oxygen.

Conventional long-term heat storage systems suffer from high losses to the environment. In a latent heat storage system based on supercooled phase change materials, there is no temperature difference between the heat storage and the environment. When heat is required, the solidification from supercooled liquid to solid can be started releasing the latent heat. This concept of thermal energy storage in supercooled liquids is still relatively unexplored. Requirements for the phase change material are high latent heat, no spontaneous nucleation and a rapid crystallization rate if fast heating is required. It was shown in this study that the crystallization velocity of supercooled xylitol can relatively easily be significantly increased with suitable additives. Still, it is very low compared to many other materials and further development is needed.

References

- [1] W. Yu, D.M. France, J. L. Routbort and S.U.S. Choi, *Heat Transfer Eng.*, 2008, **29(5)**, 432.
- [2] W. Daungthongsuk and S. Wongwises, *Renewable Sustainable Energy Rev.*, 2007, **11**, 797.
- [3] A.R. Smith, J. Klosek, *Fuel Process. Technol.*, 2001, **70**, 115.
- [4] F. G. Kerry, *Industrial Gas Handbook: Gas Separation and Purification*, CRC Press, 2007.
- [5] A. Seppälä, *Int. J. Heat and Mass Transfer*, 2012, **55**, 1582.
- [6] A. Seppälä, K. Saari and M.J. Lampinen, Factors affecting supercooling of liquids from a heat storage application perspective, TKK Applied Thermodynamics, 2008, 156, ISBN 978-951-22-9711-5. In Finnish.
- [7] X.-Q. Wang and A.S. Mujumdar, *Int. J. Therm. Sci.*, 2007, **46**, 1.
- [8] H. Sarkar, *Renewable Sustainable Energy Rev.*, 2011, **15**, 3271.
- [9] S.Z. Heris, M.N. Esfahany and S.Gh. Etemad, *Int. J. Heat Fluid Flow*, 2007, **28**, 203.
- [10] L. Godson, B. Raja, D. Mohan Lal and S. Wongwises, *Renewable Sustainable Energy Rev.*, 2010, **14**, 629.
- [11] J. Buongiorno, *J. Heat Transfer*, 2006, **128**, 240.
- [12] B.C. Pak and Y.I. Cho, *Exp. Heat Transfer*, 1998, **11**, 151.
- [13] Y. Xuan and W. Roetzel, *Int. J. Heat Mass Transfer*, 2000, **43**, 3701.
- [14] S.Z. Heris, S.Gh. Etemad and M.N. Esfahany, *Int. Commun. Heat Mass Transfer*, 2006, **33**, 529.
- [15] D. Kim, Y. Kwon, Y. Cho, C. Li, S. Cheong, Y. Hwang, J. Lee, D. Hong and S. Moon, *Curr. Appl Phys.*, 2009, **9**, 119.
- [16] R.S. Vajjha, D.K. Das and D.P. Kulkarni, *Int. J. Heat Mass Transfer*, 2010, **53**, 4607.
- [17] F.M. White, *Viscous fluid flow 3rd ed.*, McGraw-Hill, 2006.
- [18] R.W. Baker, *Ind. Eng. Chem. Res.*, 2002, **41**, 1393.
- [19] X. Feng, J. Ivory and V. Rajam, *AIChE J.*, 1999, **45**, 2142.
- [20] J. Sanchez and A. Mourgues, *J. Membr. Sci.*, 2005, **252**, 133.
- [21] J.G. Wijmans and R.W. Baker, *J. Membr. Sci.*, 1995, **107**, 1.
- [22] G. He, Y. Mi, P.L. Yue and G. Chen, *J. Membr. Sci.*, 1999, **153**, 243.
- [23] K.L. Wang, S.H. McCray, D.D. Newbold and E.L. Cussler, *J. Membr. Sci.*, 1992, **72**, 231.
- [24] S. Zhao, Z. Li, Y. Liu and L. Wang, *Desalination*, 2008, **233**, 310.
- [25] P.G. Debenetti, *Metastable Liquids – Concepts and Principles*, Princeton University Press, Princeton, 1996.
- [26] C.A. Angell, Supercooled water, in: F. Franks (Ed.), *Water – A Comprehensive Treatise*, vol. 7, Plenum Press, New York, 1982.

Paper I

A. Meriläinen, A. Seppälä, K. Saari, J. Seitsonen, J. Ruokolainen, S. Puisto, N. Rostedt and T. Ala-Nissila, *Influence of particle size and shape on turbulent heat transfer characteristics and pressure losses in water-based nanofluids*, under review in International Journal of Heat and Mass Transfer (2013).

Paper II

A. Meriläinen, A. Seppälä and P. Kauranen, *Minimizing specific energy consumption of oxygen enrichment in polymeric hollow fiber membrane modules*, Applied Energy 94 (2012).

Paper III

A. Seppälä, A. Meriläinen, L. Wikström and P. Kauranen, *The effect of additives on the speed of the crystallization front of xylitol with various degrees of supercooling*, *Experimental Thermal and Fluid Science* 34 (2010).